Available online at www.synsint.com

Synthesis and Sintering

ISSN 2564-0186 (Print), **ISSN** 2564-0194 (Online)

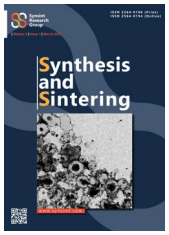

Research article

Synthesis, sintering and electrical properties of $Li_{1+x}Gd_xZr_{2-x}(PO_4)_3$ solid electrolytes for Li-ion batteries

Zahra Khakpour [a,*], **Saeed Sedaghat** [a], **Mohammad Farvizi** [a], **Nima Naderi** [b], **Abouzar Massoudi** [b]

[a] *Ceramic Department, Materials and Energy Research Center (MERC), Karaj, Iran*
[b] *Department of Semiconductors, Materials and Energy Research Center (MERC), Karaj, Iran*

ABSTRACT

In this study, the electrical characteristics of spark plasma sintered $Li_{1+x}M_xZr_{2-x}(PO_4)_3$ solid electrolytes, underlining the impacts of gadolinium (Gd) substitution on lithium-ion battery performance in comparison to conventionally sintered samples. The samples with different amounts of Gd (x= 0.1, 0.2, and 0.3) were sintered by both SPS and conventional methods and characterized using advanced techniques, including field emission scanning electron microscopy (FESEM) for microstructural analysis, X-ray diffraction (XRD) for phase detection, and energy-dispersive X-ray spectroscopy (EDS) for elemental analysis. A significant improvement in densification and a subsequent reduction in porosity are observed in the SPSed samples, which is the main reason for their enhanced structural integrity. However, this increase in densification is accompanied by a complex relationship in which the presence of Gd may hinder ionic transport compared to conventionally sintered samples. Optimizing the Gd content to balance ionic conductivity and structural stability, which supports the development of solid electrolytes for lithium-ion battery applications, was emphasized.

KEYWORDS

$Li_{1+x}Gd_xZr_{2-x}(PO_4)_3$
Electrical properties
Spark plasma sintering
Gadolinium substitution
Microstructural analysis

OPEN ACCESS

1. Introduction

In recent decades, lithium-ion batteries have gained significant commercial and scientific attention among the different metal-ion batteries. Lithium-ion batteries possess several industrial devices and portable electronic applications, including laptops, mobiles, electric vehicles, and energy grids [1, 2]. Much effort has been made to improve the performance of the new generation of lithium-ion batteries (LIBs), like improvement of their power and energy densities, enhancing their cost-effectiveness, and, more importantly, enhancing their safety for large-scale applications [3, 4].

Different safety challenges like leakage, restricted operational temperature range, and flammability can be minimized by developing the all-solid-state batteries in which the liquid electrolyte used in conventional batteries is replaced with a solid electrolyte. Additionally, using a solid electrolyte in the battery can contribute to higher energy density and a longer cycle life [2, 5, 6].

Recently, several studies have focused on the transport and structural behavior of a broad variety of inorganic solid electrolytes. Nevertheless, researchers still try to attain an optimal and affordable solid electrolyte that offers ionic conductivity comparable to that of liquid electrolytes, along with good electrochemical, mechanical, and thermal stability, and low resistance at the electrode interface for commercial applications [7, 8].

NASICON-type solid electrolytes (Li-ion conducting $Na_3Zr_2Si_2PO_{12}$) are known for their decent ionic conductivity, strong chemical stability, and relatively low interfacial resistance compared to other inorganic solid electrolytes, such as sulfides, oxides, and hydrides [9, 10].

* Corresponding author. *E-mail address:* z.khakpour@merc.ac.ir (Z. Khakpour)
Received 19 January 2024; Received in revised form 5 May 2024; Accepted 7 May 2024.

https://doi.org/10.53063/synsint.2025.51205

Table 1. Representation of the coding system of the prepared system based on their compositions.

Sample code	x	Composition
LZP	0.0	$LiZr_2(PO_4)_3$
LZPG1	0.1	$Li_{1.1}Gd_{0.1}Zr_{1.9}(PO_4)_3$
LZPG2	0.2	$Li_{1.2}Gd_{0.2}Zr_{1.8}(PO_4)_3$
LZPG3	0.3	$Li_{1.3}Gd_{0.3}Zr_{1.7}(PO_4)_3$

$LiZr_2(PO_4)_3$ (LZP) is a NASICON-type solid electrolyte, fitting the general formula $LiX_2(PO_4)_3$, where X can be Ge, Ti, or Zr. The LZP structure features a robust framework composed of corner-sharing PO_4 tetrahedra and ZrO_6 octahedra, creating a 3D network of interstitial tunnels that facilitate the easy diffusion of Li-ions [11]. Both $LiGe_2(PO_4)_3$ and $LiTi_2(PO_4)_3$ present greater ionic conductivity values compared to LZP [12]. In contrast, LZP demonstrates excellent chemical stability when in contact with Li metal, which can be attributed to the stability provided by the Zr^{4+} ion [13].

LZP has complicated polymorphism according to the starting compounds and synthesis conditions utilized for the fabrication of the material [14, 15]. The formation of LZP during synthesis is enhanced by using a higher annealing temperature (>1100 °C), resulting in its crystallization in the triclinic phase at room temperature and a transition to the rhombohedral structure at 60 °C [15]. LZP crystallized in the rhombohedral phase demonstrates the highest ionic conductivity owing to its advantageous crystal arrangement, which facilitates the rapid diffusion of Li-ions. The phase formation could be influenced by the selection of initial precursors, especially the one used for the Zr source [16]. Recent research indicates that by optimizing the sintering parameters, Zr precursor, and doping methods, LZP can be synthesized to crystallize in the rhombohedral phase at room temperature [17–19].

In the present study, $Li_{1+x}M_xZr_{2-x}(PO_4)_3$ solid electrolytes with different amounts of gadolinium (Gd) (x= 0.1, 0.2, and 0.3) are sintered by both SPS and conventional methods to study the effect of Gd on the densification and conductivity of this material.

2. Experimental

2.1. Materials and processing

To prepare the formula Li_{1+x} $M_xZr_{2-x}(PO_4)_3$ with M=Gd, stoichiometric ratios were set for x=0.1, 0.2, and 0.3, with an additive-free sample prepared as a reference. To achieve this, the raw materials —ZrO_2, Li_2CO_3, $(NH_4)_2HPO_4$, and Gd_2O_3— were weighed according to their respective weight percentages, as detailed in Table 1, and then thoroughly mixed.

The additive-free sample was prepared according to the weight percentage of the initial materials listed in Table 2. It should be mentioned that due to the high volatility of Li_2CO_3 at elevated temperatures, an additional 10 wt% was added to compensate for potential loss during processing.

Table 2. Weight percentage of the initial materials.

Raw materials	ZrO_2	Li_2CO_3	$(NH_4)_2HPO_4$
wt%	36.27	5.44	58.29

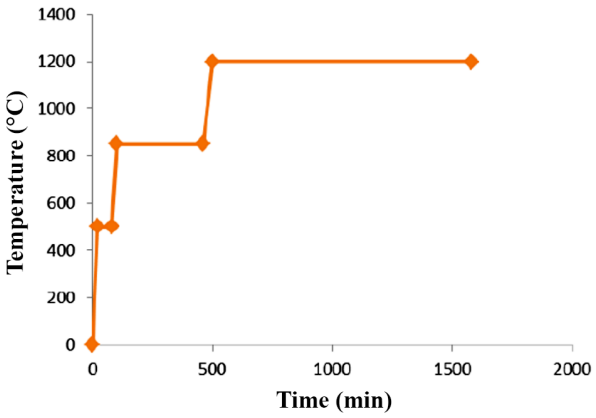

Fig. 1. Synthesis heating program of powder mixtures.

After weighing, Gd_2O_3 based on the compositions was added to powder mixtures. Then, the powders for each sample composition were mixed for 20 min using a tubular mixer. Then, to dehydrate the mixed powder from the absorbed water, the mixtures were poured into 100 cc alumina crucibles and placed in an oven at 110 °C for 4 h. In the next step, the obtained powder mixtures were dry milled using zirconia cups and balls in a planetary ball mill for 1 h at 220 rpm speed. Then, the four obtained powder mixtures were poured into four alumina crucibles and placed inside a box furnace with an air atmosphere to carry out the synthesis process, as outlined in Fig. 1.

After completion of the heating program, the furnace was turned off and allowed to gradually decrease the internal temperature and slowly anneal to ambient conditions. Then, the synthesized powders were removed from the oven. Due to the phosphate nature of the compounds, the powders formed as puffs during the process, likely due to the release of gases. Fig. 2 displays one of the ceramic crucibles removed from the furnace. After the synthesized powders were separated from the ceramic crucibles, they were milled in a planetary ball mill for 1 h at a speed of 300 rpm and then passed through a 400-mesh sieve. The obtained powders, with particle sizes less than 37 μm, were prepared for shaping and further analysis.

Fig. 2. One of the ceramic crucibles including synthesized powder removed from the furnace.

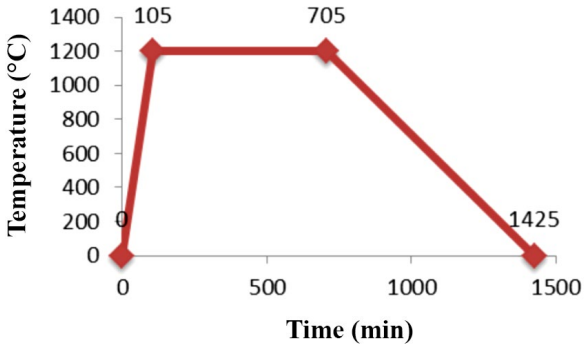

Fig. 3. Heating program of furnace after pressing.

After synthesizing the powders, coin-shaped samples were prepared from each composition by applying an initial pressure of 10 MPa and a final pressure of 80–100 MPa using a uniaxial hydraulic press. The samples had a diameter of 13 mm and a thickness of 8–9 mm. The prepared coin-shaped samples were placed in alumina crucibles and sintered in a box furnace (Amalgam model, Iran) according to the temperature program illustrated in Fig. 3. The sintering of the samples was carried out using the muffle method in a powder bed to minimize contamination and the release of volatile substances.

To manufacture the samples using the spark plasma sintering method, it was anticipated, based on references, that LZPG3 would yield the best results. Therefore, due to economic constraints, only LZP and LZPG3 were selected for spark plasma sintering. LZP and LZPG3 powders were loaded into a graphite mold lined with thin, flexible graphite foil to prevent sticking and chemical reactions between the mold and the powders. The sintering process was performed at the temperature 1200 °C for a dwell time of 20 min under a mechanical pressure of 30 MPa in a vacuum.

2.2. Characterization

The densities of the synthesized powders were measured by glass pycnometer based on the EN 1097-6. The bulk densities of the sintered samples were measured using the Archimedes method. The relative densities were then calculated by dividing the measured bulk densities by the theoretical densities. The crystalline phases of both the synthesized powders and the as-sintered samples were identified using X-ray diffraction (XRD, Philips PW3710) analysis. The morphology of the synthesized powders and the microstructure of the as-sintered specimens were examined using field emission scanning electron microscopy (FESEM, Tescan S8000). Elemental composition analysis was conducted using energy-dispersive X-ray spectroscopy (EDS). In addition, conductivity measurements were conducted using an impedance analyzer (Autolab-PGstate30) on the polished samples, which were coated with gold by magnetron sputtering for their high electrical conductivity.

Table 3. Measured densities of synthesized powders.

Sample code	Density (g/cm^3)
LZP	2.6634
LZPG1	2.6113
LZPG2	2.6066
LZPG3	2.6010

3. Results and discussion

3.1. Synthesized powder samples

The results of XRD analysis of synthesized powders are illustrated in Fig. 4. As seen in Fig. 4, the sharp peaks with strong intensity indicate that the synthesized powders are fully crystalline, with no presence of amorphous phases. Since the synthesis procedure was carried out at a temperature of 1200 °C, it appears that the resulting compositions exhibit both rhombohedral ($R\bar{3}c$) and monoclinic (C2/c) crystal structures [20]. It should be noted that due to the high ionic conductivity of the rhombohedral structure (NASiCON), this structure is the preferred one for the synthesized powders. Based on the XRD pattern of the LZP sample, the peaks of the synthesized $LiZr_2(PO_4)_3$ show good alignment with the peaks in JCPDS card no. 00-33-777. However, the peaks are slightly shifted to the right, likely due to the diffusion of elements from the raw materials into the microstructure, leading to an increase in the lattice spacing d according to Hooke's Law (Eq. 1).

$$\lambda = 2d \sin\theta \quad (1)$$

As shown in Fig. 4, peaks corresponding to gadolinium phosphate have appeared in the XRD patterns of the synthesized samples. As the Gd content increases in the compositions, the intensity of the peaks related

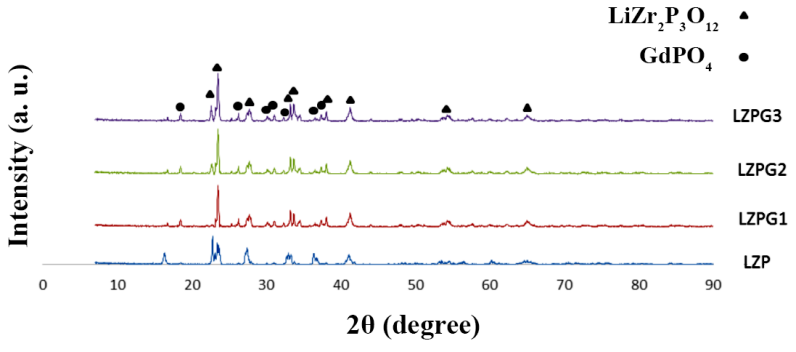

Fig. 4. XRD patterns of synthesized powders.

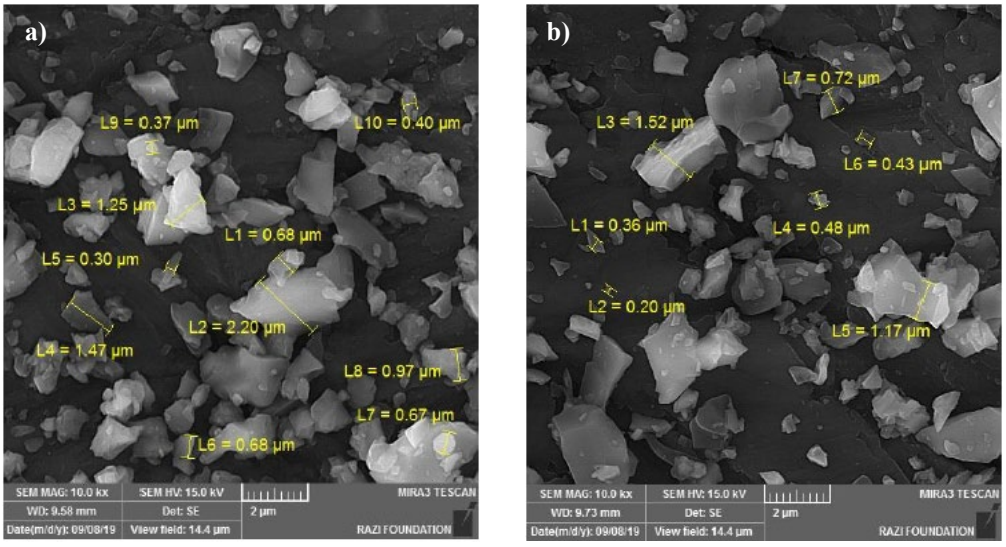

Fig. 5. FESEM images of the synthesized a) LZP and b) LZPG3 powders.

to the rhombohedral structure also increases. However, since the number of additives is relatively small, the increase in intensity is not significant and can only be observed in the main peaks. A small amount of ZrO_2 has also been detected in the synthesized powders.

Fig. 5 presents FESEM images of the synthesized LZP and LZPG3 powders. It is evident that the particle sizes are in the micron range and lack any specific shape.

The densities of the synthesized samples, measured using a pycnometer, are listed in Table 3. As can be observed, the densities of the powder samples decrease as the content of additive increases. On one hand, adding metallic elements and substituting them for zirconium increases the atomic weight of the unit cell. On the other hand, due to the high atomic radius of these elements (see Table 4), the volume of the unit cell also increases. However, the increase in unit cell volume is more significant compared to the increase in atomic weight due to the incorporation of Gd elements. Therefore, the densities of the powders decrease as the additive content increases.

3.2. Sintered samples

The sintering behavior of the samples can be explained by plotting a diagram of displacement (sample thickness) versus sintering time. Fig. 6 shows the diagram of sample thickness versus sintering time for the LZP sample, which was sintered at a temperature of 1200 °C for a soaking time of 20 min. As can be seen in Fig. 6, there is a reduction in the sample thickness within the first 2 minutes of the process. Since the heating process has just started during this period, this displacement is attributed to the application of mechanical pressure. Afterward, the thickness of the sample remains constant up to the 12th minute. Then, as the electric current increases, the Joule heating mechanism is activated in the powder particles, which leads to the rearrangement of the particles. This rearrangement helps to fill the pores and reduce the porosities, which in turn reduces the thickness of the sample. In addition, according to the ohmic heating mechanism, creating heat through the resistance of the material, the sparks generated between particles and the creation of plasma contribute to neck formation, further promoting the sintering process. At this stage, the plasma formation causes the temperature at the grain interface to rise suddenly to about 10,000 °C, which leads to the melting of the particle surfaces and subsequent necking [25]. After necking, the ohmic mechanism (responsible for spark generation) is disabled, leaving only the Joule heating mechanism to continue densification. This stage plays a critical role in increasing the density. The final step of densification is related to grain growth, which begins around the 35th minute, but it is negligible [26, 27].

Table 4. Atomic characteristics of zirconium and gadolinium.

Element	Atomic weight (g/mol)	Atomic radius (nm)
Zr	91.24 [21]	158 [22]
Gd	157.25 [23]	180 [24]

Table 5 lists the bulk density, relative density, and total porosity of pressed and SPSed samples measured based on the Archimedes method. As observed, the SPSed samples possess higher relative densities compared to those of the pressed samples. On the other hand, the relative density of samples increases as the amount of additive increases. The improvement in densification can be attributed to the formation of a glassy phase that enhances the sinterability of the powders, as well as the higher atomic weight of the additive elements compared to zirconium, which leads to an increase in the specific weight.

Fig. 7 presents the results of the XRD analysis, which were used to identify the phase composition of the SPSed samples. As expected, the intensity of the XRD peaks increased, indicating greater order and alignment of the grains. In the additive-free sample, the $LiZr_2(PO_4)_3$ phase with a rhombohedral structure ($R\bar{3}c$) is identified, as referenced in JCPDS card no. 96-400-0263. As observed, not only did the intensity of the rhombohedral structure increase, but the additional peaks corresponding to the gadolinium phosphate phase formed during the SPS method appeared.

The FESEM images of fractured surfaces of SPSed samples are shown in Fig. 8. As can be seen in Fig. 8a, the porosity of the LZP sample is consistent with the calculated relative density of 86.47%. However,

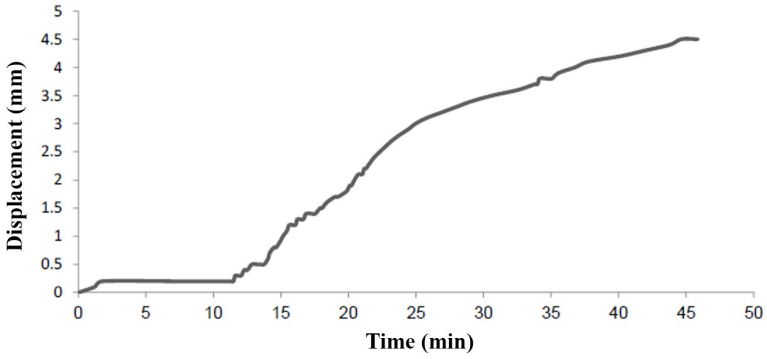

Fig. 6. The displacement-time diagram of SPSed LZP.

good connection and necking between the particles can be observed, indicating that sintering progressed, but the porosity was not eliminated due to insufficient temperature. It can be seen in Fig. 8b that the addition of Gd has led to the elimination of porosity and consequently increased the relative density to 94.62%. A more integrated microstructure is observed where the grains are in full contact with each other and the porosity is reduced, indicating improved sinterability and a positive effect of the additive. However, grain growth appears to have occurred due to the addition of the additive.

The backscattered FESEM image and the EDS spectrum of the SPSed LZPG3 sample are shown in Fig. 9. In the image, the distinct color contrast between regions A and B indicates a phase difference at these points. As can be seen, the accumulation of the Gd element is more significant at this point compared to point A. In contrast, this point appears to be either free of Zr or contain only a very small amount. It can be inferred that point A, which has a lighter color, corresponds to the gadolinium phosphate phase, while phase B is related to $LiZr_2(PO_4)_3$.

Fig. 10 presents the FESEM images of the fracture surface of the pressed and conventionally sintered samples. As observed, the sintering process has advanced, and the necks between the grains are visible. Additionally, as shown in Table 5, these samples exhibit relatively high porosity, which is also evident in the FESEM images. Although both series of samples were sintered at the same temperature, the absence of applied pressure during the sintering process resulted in a higher residual porosity in these samples compared to the SPSed samples. Comparing Figs. 8a & 10a, it is evident that sintering the LZP sample using the SPS method prevented excessive grain growth, resulting in a finer microstructure compared to conventional sintering. Additionally, the formation of plasma and the distinct sintering mechanism in the SPS furnace further contributed to improved sintering and densification.

The backscattered FESEM image from the polished surface of the LZP sample sintered by the conventional method, along with the EDS energy dispersive spectrum, is shown in Fig. 11. The color contrast between points A and B in Fig.11 indicates a phase difference, with the constituent elements identified through EDS analysis. Point A has a higher zirconium content than point B, indicating a concentration of zirconium oxide particles. The dark region at point B can be attributed to $LiZr_2(PO_4)_3$.

To identify the elements constituting the various phases present in the cold-pressed and conventionally sintered LZPG3 sample, EDS analysis was performed, as shown in Fig. 12. As expected, point A, which appears as the lighter phase, has a higher Gd content and lower Zr content compared to the darker phase (point B), indicating the presence of a gadolinium phosphate phase in this region. Based on the elemental distribution in phase B and previous discussions, this phase is likely related to $LiZr_2(PO_4)_3$.

All samples were tested using a potentiostat to determine their electrical conductivity through Nyquist plot analysis. The curves were processed using ZView software, and the ionic resistances were calculated. Fig. 13 presents the Nyquist plots for the SPSed samples. The first semicircle typically corresponds to the intrinsic response of the grain. For the LZP sample shown in Fig. 13a, this is likely associated with ionic conductivity within the grains. The second semicircle with an additional arc may indicate the grain boundary

Table 5. Bulk density, relative density, and total porosity of pressed and SPSed samples.

Sample	Bulk density (g/cm^3)	Relative density (%)	Total porosity (%)
LZP (Pressed)	2.0271	76.11	23.89
LZPG1 (Pressed)	2.0478	78.42	21.58
LZPG2 (Pressed)	2.0496	78.63	21.37
LZPG3 (Pressed)	2.1076	81.03	18.9
LZP (SPSed)	2.3030	86.47	13.53
LZPG3 (SPSed)	2.4663	94.62	5.38

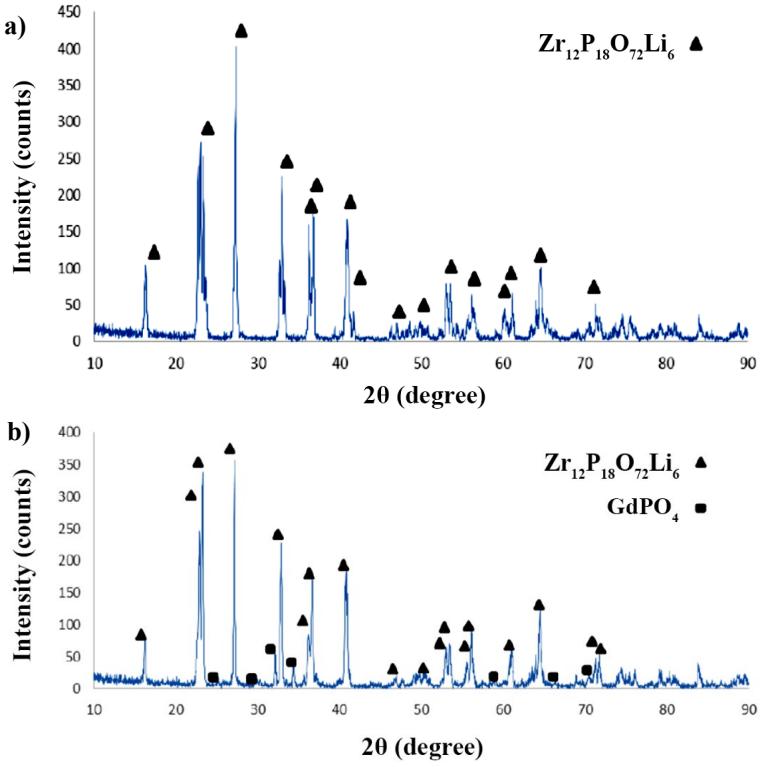

Fig. 7. XRD results of SPSed a) LZP and b) LZPG3.

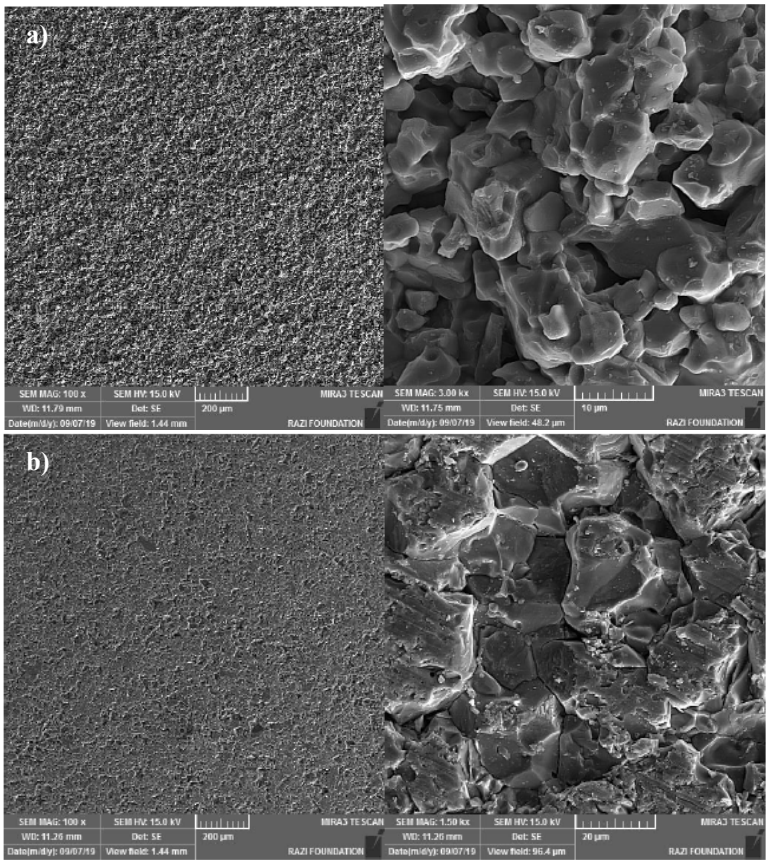

Fig. 8. FESEM images of fractured surfaces of SPSed samples a) LZP and b) LZPG3.

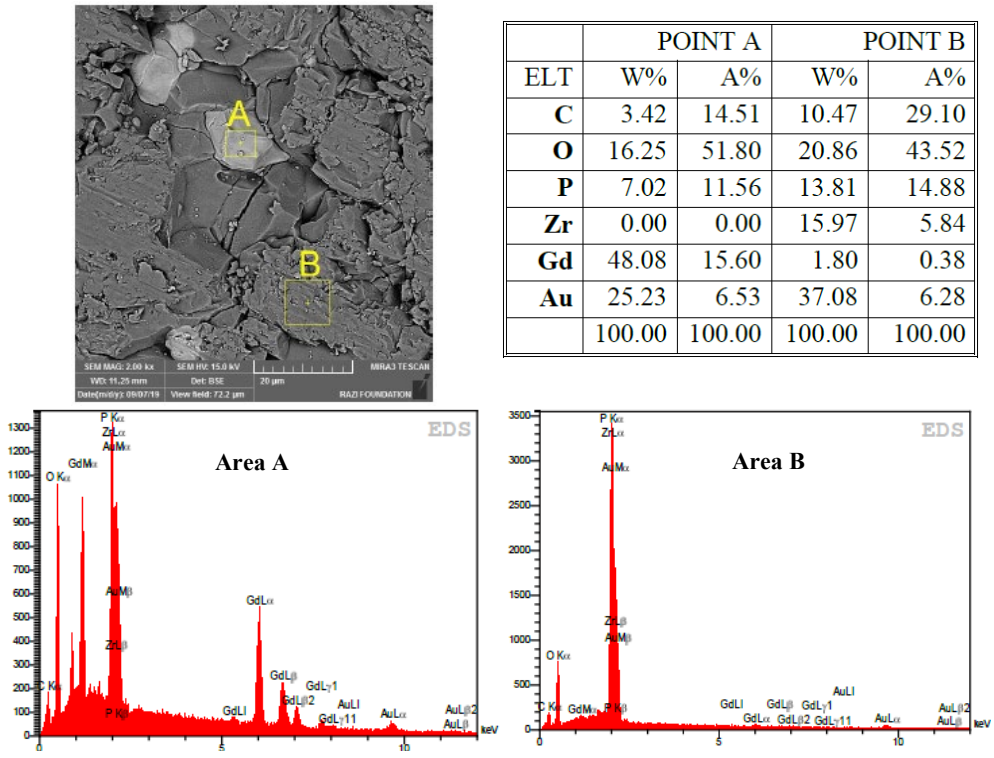

	POINT A		POINT B	
ELT	W%	A%	W%	A%
C	3.42	14.51	10.47	29.10
O	16.25	51.80	20.86	43.52
P	7.02	11.56	13.81	14.88
Zr	0.00	0.00	15.97	5.84
Gd	48.08	15.60	1.80	0.38
Au	25.23	6.53	37.08	6.28
	100.00	100.00	100.00	100.00

Fig. 9. The backscattered FESEM image and EDS analysis of SPSed LZPG3.

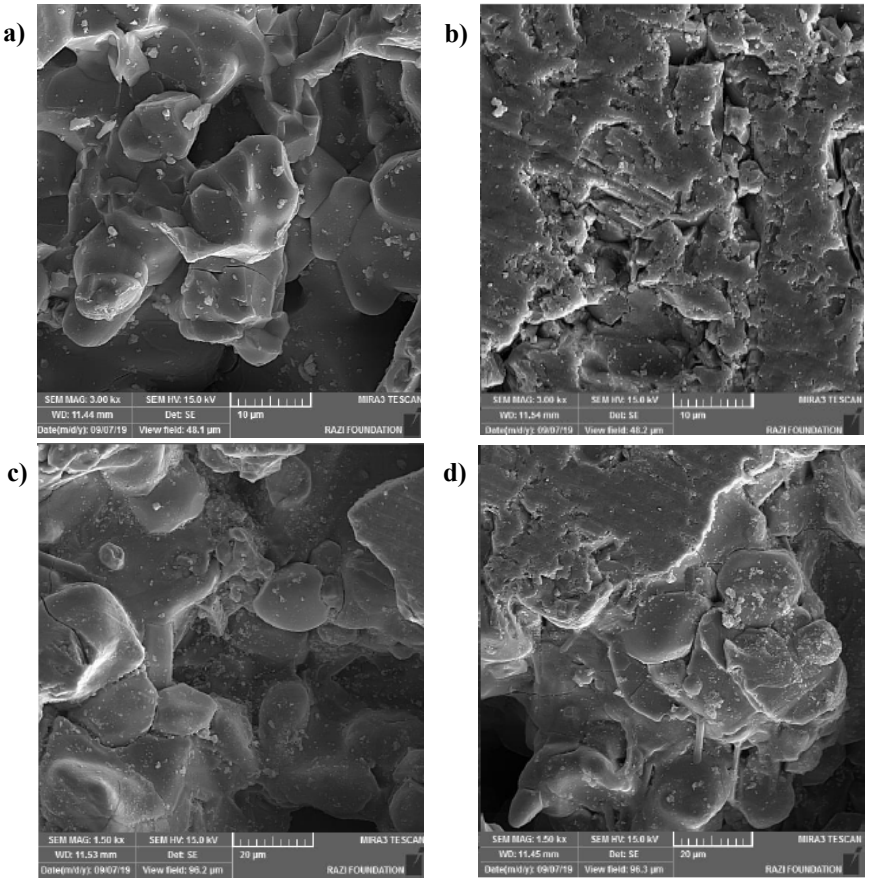

Fig. 10. FESEM images of sintered a) LZP, b) LZPG, c) LZPG2, and d) LZPG3.

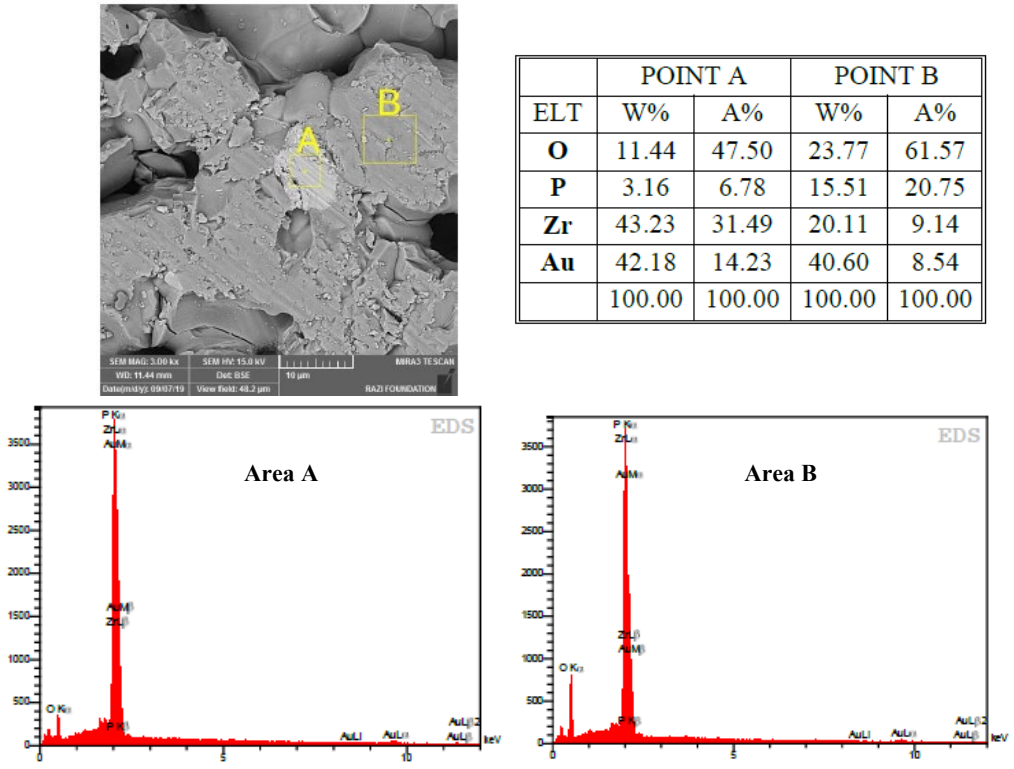

	POINT A		POINT B	
ELT	W%	A%	W%	A%
O	11.44	47.50	23.77	61.57
P	3.16	6.78	15.51	20.75
Zr	43.23	31.49	20.11	9.14
Au	42.18	14.23	40.60	8.54
	100.00	100.00	100.00	100.00

Fig. 11. EDS analysis of sintered LZP.

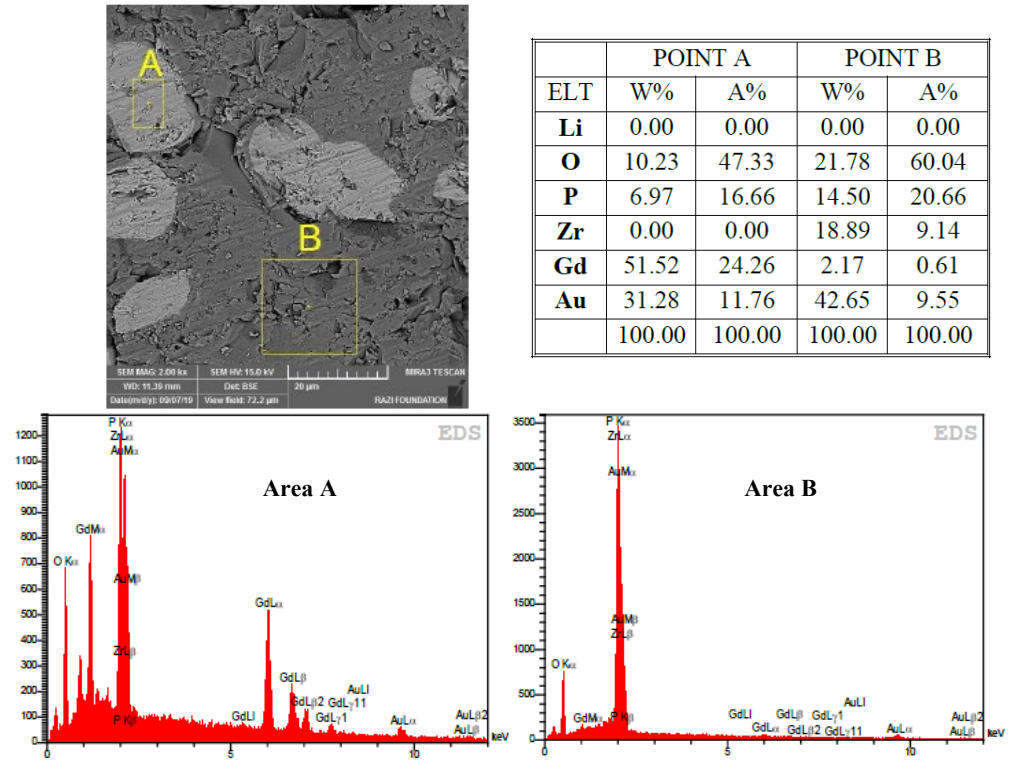

	POINT A		POINT B	
ELT	W%	A%	W%	A%
Li	0.00	0.00	0.00	0.00
O	10.23	47.33	21.78	60.04
P	6.97	16.66	14.50	20.66
Zr	0.00	0.00	18.89	9.14
Gd	51.52	24.26	2.17	0.61
Au	31.28	11.76	42.65	9.55
	100.00	100.00	100.00	100.00

Fig. 12. EDS analysis of sintered LZPG3.

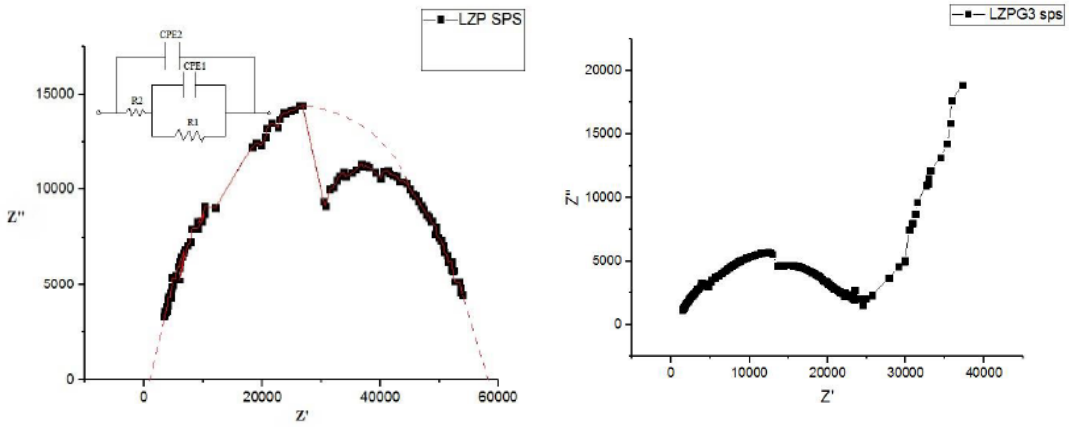

Fig. 13. Nyquist plots of SPSed LZP and LZPG3.

resistance. In many ceramics, grain boundaries exhibit higher resistivity than the grain interiors. Any streaks or lines on the low-frequency side of the Nyquist plot may indicate a diffusion process, potentially associated with the movement of lithium ions across grain boundaries or through the pores of the material.

Fig. 13b shows the Nyquist plot for LZPG3. The addition of Gd appears to increase both intra-grain and grain boundary resistivity. Gd may influence the crystal structure or introduce local regions with varying ionic conductivity, potentially hindering the movement of Li^+ ions. Gd can segregate at grain boundaries, thereby increasing boundary resistance, similar to other impurities that may enhance or hinder conductivity depending on their concentration and distribution. In the $LiZr_2$ $(PO_4)_3$ matrix, the presence of Gd appears to increase overall impedance, particularly affecting grain boundaries. This could represent a trade-off, where Gd may enhance certain properties (such as stability or magnetic characteristics) but at the cost of reduced ionic conductivity.

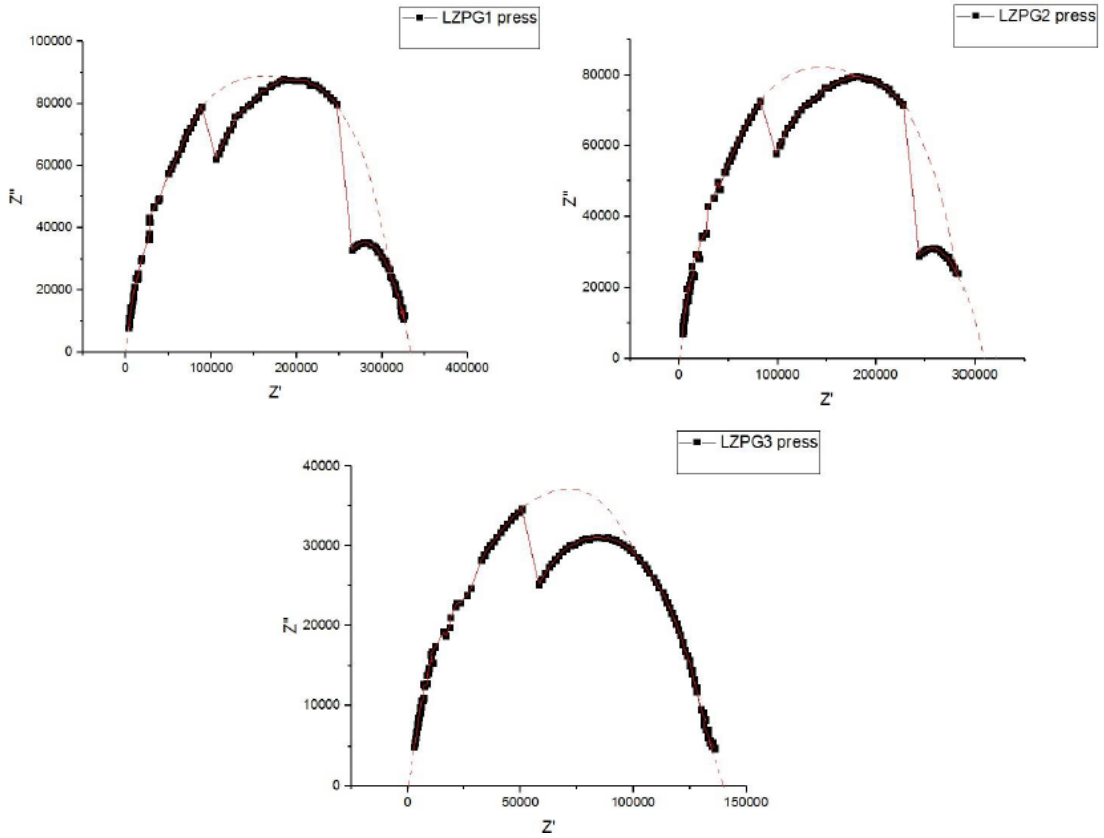

Fig. 14. Nyquist plots of sintered LZPG1, LZPG2, and LZPG3.

Fig. 14 shows the Nyquist curves for the conventionally sintered samples. The semicircular shape of the curves indicates similar frequency-dependent behavior among the samples. The LZPG1 sample exhibits a larger semicircle, suggesting higher resistance. With increasing Gd content (LZPG2 and LZPG3), the size of the semicircles decreases, indicating a reduction in resistance. As previously discussed, higher Gd content leads to increased sample density and reduced porosity, which may contribute to the observed decrease in resistance. These structural changes directly influence the impedance behavior of the samples. As Gd content increases, improved grain-to-grain contact due to higher density creates more efficient ionic conduction paths, thereby reducing internal resistance. This is reflected in the Nyquist plots as a decrease in the size of the semicircles. Porosity reduction also minimizes barriers to ion movement within the material. With fewer and smaller pores, ions can traverse the structure more easily, resulting in lower electrical resistance and enhanced ionic conductivity.

4. Conclusions

This study provides valuable insights into the synthesis and electrical properties of $Li_{1+x}Gd_xZr_{2-x}(PO_4)_3$ solid electrolytes, which are critical for the development of high-performance lithium-ion batteries. The comparative analysis of SPS and conventional sintering techniques revealed that SPS significantly enhances densification and reduces porosity, leading to improved ionic conductivity. However, the incorporation of gadolinium (Gd) into the structure, while beneficial in some aspects, was found to affect ionic transport. This highlights the importance of optimizing Gd content to achieve an ideal balance between enhancing ionic conductivity and maintaining structural stability. Overall, the findings underscore the potential of tailored solid electrolytes in advancing lithium-ion battery technology, paving the way for more efficient and reliable energy storage solutions.

CRediT authorship contribution statement

Zahra Khakpour: Project administration, Supervision.
Saeed Sedaghat: Writing – original draft, Investigation.
Mohammad Farvizi: Formal analysis, Conceptualization.
Nima Naderi: Methodology, Writing – review & editing.
Abouzar Massoudi: Data curation, Writing – review & editing.

Data availability

The data underlying this article will be shared on reasonable request to the corresponding author.

Declaration of competing interest

The authors declare no competing interests.

Funding and acknowledgment

This work was extracted from the master's thesis of the second author. The authors gratefully acknowledge the Materials and Energy Research Center (MERC) for providing the necessary materials and equipment. This research was supported under grant number RA-14-1-A.

References

[1] Y. Shao, F. Ding, J. Xiao, J. Zhang, W. Xu, et al., Making Li-Air Batteries Rechargeable: Material Challenges, Adv. Funct. Mater. 23 (2013) 987–1004. https://doi.org/10.1002/adfm.201200688.
[2] Q. Zhao, S. Stalin, C.-Z. Zhao, L.A. Archer, Designing solid-state electrolytes for safe, energy-dense batteries, Nat. Rev. Mater. 5 (2020) 229–252. https://doi.org/10.1038/s41578-019-0165-5.
[3] E. Quartarone, P. Mustarelli, Electrolytes for solid-state lithium rechargeable batteries: recent advances and perspectives, Chem. Soc. Rev. 40 (2011) 2525. https://doi.org/10.1039/c0cs00081g.
[4] J.B. Goodenough, Y. Kim, Challenges for Rechargeable Li Batteries, Chem. Mater. 22 (2010) 587–603. https://doi.org/10.1021/cm901452z.
[5] A. Manthiram, X. Yu, S. Wang, Lithium battery chemistries enabled by solid-state electrolytes, Nat. Rev. Mater. 2 (2017) 16103. https://doi.org/10.1038/natrevmats.2016.103.
[6] B. Dunn, H. Kamath, J.-M. Tarascon, Electrical Energy Storage for the Grid: A Battery of Choices, Science. 334 (2011) 928–935. https://doi.org/10.1126/science.1212741.
[7] J. Janek, W.G. Zeier, A solid future for battery development, Nat. Energy. 1 (2016) 16141. https://doi.org/10.1038/nenergy.2016.141.
[8] N. Kamaya, K. Homma, Y. Yamakawa, M. Hirayama, R. Kanno, et al., A lithium superionic conductor, Nat. Mater. 10 (2011) 682–686. https://doi.org/10.1038/nmat3066.
[9] Z. Jian, Y. Hu, X. Ji, W. Chen, NASICON-Structured Materials for Energy Storage, Adv. Mater. 29 (2017) 1601925. https://doi.org/10.1002/adma.201601925.
[10] F. Zheng, M. Kotobuki, S. Song, M.O. Lai, L. Lu, Review on solid electrolytes for all-solid-state lithium-ion batteries, J. Power Sourc. 389 (2018) 198–213. https://doi.org/10.1016/j.jpowsour.2018.04.022.
[11] B.E. Francisco, C.R. Stoldt, J.-C. M'Peko, Lithium-Ion Trapping from Local Structural Distortions in Sodium Super Ionic Conductor (NASICON) Electrolytes, Chem. Mater. 26 (2014) 4741–4749. https://doi.org/10.1021/cm5013872.
[12] M. Hou, F. Liang, K. Chen, Y. Dai, D. Xue, Challenges and perspectives of NASICON-type solid electrolytes for all-solid-state lithium batteries, Nanotechnology. 31 (2020) 132003. https://doi.org/10.1088/1361-6528/ab5be7.
[13] Y. Zhang, K. Chen, Y. Shen, Y. Lin, C.-W. Nan, Enhanced lithium-ion conductivity in a LiZr2(PO4)3 solid electrolyte by Al doping, Ceram. Int. 43 (2017) S598–S602. https://doi.org/10.1016/j.ceramint.2017.05.198.
[14] M. Harada, H. Takeda, S. Suzuki, K. Nakano, N. Tanibata, et al., Bayesian-optimization-guided experimental search of NASICON-type solid electrolytes for all-solid-state Li-ion batteries, J. Mater. Chem. A. 8 (2020) 15103–15109. https://doi.org/10.1039/D0TA04441E.
[15] H. Xu, S. Wang, H. Wilson, F. Zhao, A. Manthiram, Y-Doped NASICON-type LiZr2(PO4)3 Solid Electrolytes for Lithium-Metal Batteries, Chem. Mater. 29 (2017) 7206–7212. https://doi.org/10.1021/acs.chemmater.7b01463.
[16] Y. Li, W. Zhou, X. Chen, X. Lü, Z. Cui, et al., Mastering the interface for advanced all-solid-state lithium rechargeable batteries, Proc. Natl. Acad. Sci. 113 (2016) 13313–13317. https://doi.org/10.1073/pnas.1615912113.
[17] S. Khatua, Y.B. Rao, K.R. Achary, L.N. Patro, Li-ion transport studies of NASICON-type LiZr2(PO4)3 solid electrolyte crystallizing in rhombohedral structure at room temperature, Surf. Interfaces. 41 (2023) 103212. https://doi.org/10.1016/j.surfin.2023.103212.
[18] S. Kumar, P. Balaya, Improved ionic conductivity in NASICON-type Sr2+ doped LiZr2(PO4)3, Solid State Ion. 296 (2016) 1–6. https://doi.org/10.1016/j.ssi.2016.08.012.
[19] V. Ramar, S. Kumar, S.R. Sivakkumar, P. Balaya, NASICON-type La3+substituted LiZr2(PO4)3 with improved ionic conductivity as

solid electrolyte, Electrochim. Acta. 271 (2018) 120–126. https://doi.org/10.1016/j.electacta.2018.03.115.
[20] M. Catti, Lithium location in NASICON-type Li+ conductors by neutron diffraction. I. Triclinic α′-LiZr2(PO4)3, Solid State Ion. 123 (1999) 173–180. https://doi.org/10.1016/S0167-2738(99)00089-2.
[21] F.W. Aston, The isotopic constitution and atomic weights of hafnium, thorium, rhodium, titanium, zirconium, calcium, gallium, silver, carbon, nickel, cadmium, iron and indium, Proc. R. Soc. London. Ser. A - Math. Phys. Sci. 149 (1935) 396–405. https://doi.org/10.1098/rspa.1935.0070.
[22] V.M.S. Muthaiah, S. Mula, Effect of zirconium on thermal stability of nanocrystalline aluminium alloy prepared by mechanical alloying, J. Alloys Compd. 688 (2016) 571–580. https://doi.org/10.1016/j.jallcom.2016.07.038.
[23] M.E. Wieser, Atomic weights of the elements 2005 (IUPAC Technical Report), Pure Appl. Chem. 78 (2006) 2051–2066. https://doi.org/10.1351/pac200678112051.
[24] C. Boshui, D. Junxiu, C. Guoxu, Tribochemistry of gadolinium dialkyldithiophosphate, Wear. 196 (1996) 16–20. https://doi.org/10.1016/0043-1648(95)06821-X.
[25] D. Demirskyi, H. Borodianska, D. Agrawal, A. Ragulya, Y. Sakka, O. Vasylkiv, Peculiarities of the neck growth process during initial stage of spark-plasma, microwave and conventional sintering of WC spheres, J. Alloys Compd. 523 (2012) 1–10. https://doi.org/10.1016/j.jallcom.2012.01.146.
[26] M.I. Kimpa, M.Z.H. Mayzan, J.A. Yabagi, M.M. Nmaya, K.U. Isah, M.A. Agam, Review on Material Synthesis and Characterization of Sodium (Na) Super-Ionic Conductor (NASICON), IOP Conf. Ser. Earth Environ. Sci. 140 (2018) 012156. https://doi.org/10.1088/1755-1315/140/1/012156.
[27] A. Jonderian, E. McCalla, The role of metal substitutions in the development of Li batteries, part II: solid electrolytes, Mater. Adv. 2 (2021) 2846–2875. https://doi.org/10.1039/D1MA00082A.